Electron–cyclotron damping of helicon waves in low diverging magnetic fields

T. Lafleur, C. Charles, and R. W. Boswell

Citation: Phys. Plasmas **18**, 043502 (2011); doi: 10.1063/1.3573864
View online: http://dx.doi.org/10.1063/1.3573864
View Table of Contents: http://pop.aip.org/resource/1/PHPAEN/v18/i4
Published by the American Institute of Physics.

Electron–cyclotron damping of helicon waves in low diverging magnetic fields

T. Lafleur,[a] C. Charles, and R. W. Boswell,
Space Plasma, Power and Propulsion Group, Research School of Physics and Engineering, The Australian National University, Canberra, ACT 0200, Australia

(Received 17 January 2011; accepted 5 March 2011; published online 15 April 2011)

Particle-in-cell simulations are performed to investigate wave propagation and absorption behavior of low-field ($B_0 < 5$ mT) helicon waves in the presence of a diverging magnetic field. The 1D electromagnetic simulations, which include experimental external magnetic field profiles, provide strong evidence for electron–cyclotron damping of helicon waves in the spatially decaying nonuniform magnetic field. For a dipole-type magnetic field configuration, the helicon waves are absence in the downstream (lower field) region of the plasma and are observed to be completely absorbed. As the magnetic field is changed slightly however, wave damping decreases, and waves are able to propagate freely downstream, confirming previous experimental measurements of this phenomenon. © *2011 American Institute of Physics*. [doi:10.1063/1.3573864]

I. INTRODUCTION

Helicons are right-hand polarized (RHP) electromagnetic (EM) waves that propagate in bounded magnetized plasmas for frequencies above the ion cyclotron, and, if electron inertia effects are included, up to the electron cyclotron frequency.[1] Helicon wave discharges are associated with high ionization rates and are often able to produce plasma densities in excess of 10^{20} m^{-3}.[1] For helicon waves to propagate, an external magnetic field, B_0, is required, with typical strengths of tens to hundreds of millitesla. In many helicon reactors, as this external magnetic field is increased from zero (for a fixed neutral gas pressure and rf power input), a distinct density peak is observed at very low magnetic fields[2,3] (1 mT $< B_0 <$ 5 mT); lower than that used in typical helicon discharges.[1] This suggests an increased ionization efficiency, since the magnetic field is too low for significant plasma confinement to occur.

Accompanying the formation of these low-field density peaks are often corresponding peaks in the antenna loading resistance,[4,5] suggesting that the density increase is due to an enhanced antenna/plasma coupling efficiency. Numerical studies[6,7] suggest that these resistance peaks can be related to wave reflection at boundaries for some types of antennas and that the plasma resistance is large for certain wave eigenmodes, leading to possible peaks at low magnetic fields depending on the antenna configuration.

Recent experiments[8] in low diverging magnetic fields have shown wave "trapping" phenomena that are absent from previous studies of low-field helicons,[3,4] which typically use uniform magnetic fields. In these experiments,[8] waves were observed in the upstream source region of the reactor but were absent in the downstream region. Wave propagation in the downstream region was, however, observed by changing the magnitude of the magnetic field near the source exit. Because of the diverging magnetic field, the magnitude of the field at this location gives electron cyclotron frequencies close to the wave frequency. Helicon waves cannot propagate past such a cyclotron resonance point,[1] and it thus appears as if waves are either being reflected or rapidly attenuated due to electron–cyclotron damping.[9,10] Cyclotron damping is a process where electrons can collisionlessly absorb power from an electromagnetic wave and occurs when the electron cyclotron frequency is close to the wave frequency (due to Doppler-shifting effects though, this region can be quite broad[9–11]), so that electrons effectively "see" a static wave electric field.

A simple analytical model based on the warm plasma dispersion relation was developed,[8] suggesting cyclotron damping could be a feasible mechanism to explain the wave trapping observations, but this relation assumes a uniform magnetic field and plasma density, which are not true in the experiment. In this paper, a 1D electromagnetic particle-in-cell PIC simulation that we have developed is used to simulate the original experimental reactor,[8] and together with experimentally measured density and magnetic field profiles, helicon wave propagation is investigated and compared with the results of previous[8] measurements made with a B-dot probe. The simulation results provide strong evidence to support electron–cyclotron damping as the mechanism responsible for the previously observed wave trapping[8] and demonstrates an additional electron heating process in low magnetic fields that is usually absent in typical helicon discharges.

II. DESCRIPTION OF MODEL

The *Piglet* helicon reactor used in the previous wave studies[8] is shown schematically in Fig. 1(a). The system has a 20 cm long Pyrex source tube connected to a larger aluminium diffusion chamber. An rf double-saddle field antenna, 10 cm long, surrounds the source tube and is used to produce the plasma (and launch helicon waves). The antenna is connected to an rf power generator (operated at 13.56 MHz and 250 W) and a matching network. *Piglet* makes use of two

[a]Electronic mail: trevor.lafleur@anu.edu.au.

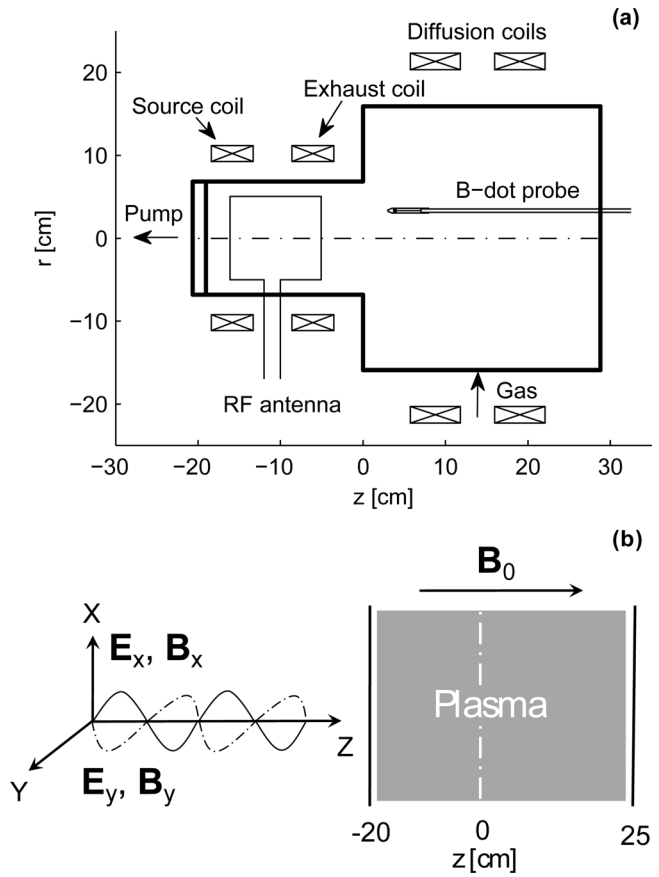

FIG. 1. (a) Schematic of the *Piglet* helicon reactor including the source region ($z < 0$ cm), diffusion chamber ($z > 0$ cm), magnetic field coils, and B-dot probe. (b) Schematic of the 1D PIC model. Right-hand polarized waves enter from the left where they propagate in the magnetized plasma located between the boundaries at $z = -20$ cm and $z = 25$ cm. An external magnetic field, B_0, is applied parallel to the simulation direction.

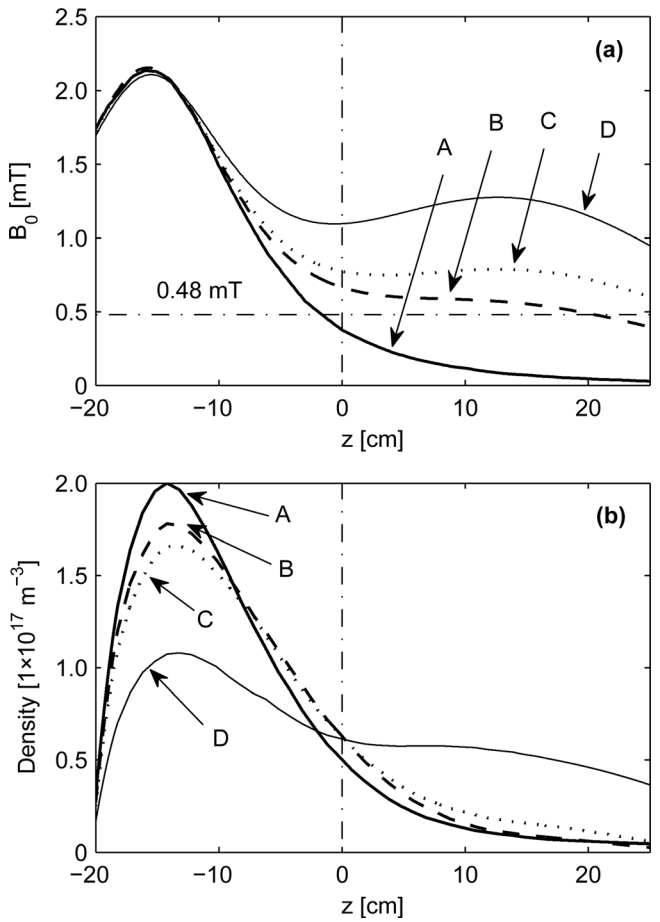

FIG. 2. (a) Axial profiles within *Piglet* of the magnetic field configurations used in the previous experimental investigation (Ref. 8). The vertical dashed line shows the location of the source tube exit in *Piglet*, while the horizontal dashed line shows the magnetic field strength giving an electron cyclotron frequency equal to the helicon wave frequency of 13.56 MHz. (b) Measured axial density profiles for the magnetic field configurations in (a). The vertical dashed line shows the location of the source tube exit in *Piglet*. The magnetic field configurations, together with the density measurements, are experimental profiles that have been presented previously in Ref. 8.

pairs of magnetic field coils. The first pair surrounds the source tube and antenna, with each coil consisting of approximately 500 turns. The second pair surrounds the diffusion chamber, with each coil having about 280 turns. All previous experiments were conducted with argon at a working pressure of 0.08 Pa.

To simulate the *Piglet* reactor, a 1D geometry is used for the PIC model. This type of model allows most of the essential physics to be captured and avoids the added complexity that results when trying to simulate and diagnose in 2D. The 1D geometry used is showed in Fig. 1(b). Here, a RHP wave is launched from the left-hand side (LHS) boundary and enters a plasma-filled box of length $L = 45$ cm. The wave then travels in the plasma, suffering possible reflections and/or absorption before reaching the right-hand side (RHS) boundary. At this point, the wave either reenters the plasma due to reflections or exits. The EM waves are excited with a frequency of 13.56 MHz (except where otherwise stated) and are assumed to propagate parallel to the simulation direction (and applied magnetic field), so that the perpendicular wave numbers, k_x and k_y, are zero.

An external magnetic field ($B_z = B_0$) is applied parallel to the simulation direction and has an axial profile matching that of the magnetic field test cases used in the previous experimental investigation.[8] In this previous investigation,[8] wave propagation in a low-field helicon mode was investigated with a number of external magnetic field configurations, produced using a combination of the magnetic field coils shown in Fig. 1(a). The axial profiles of the B_z component of these magnetic field configurations are shown in Fig. 2(a), together with the corresponding axial density profiles [Fig. 2(b)] measured with a Langmuir probe for these cases. Ions in the plasma are considered immobile and are loaded with a constant density profile matching those in Fig. 2(b) (which have been extrapolated for $z > 18$ cm and $z < -17$ cm). The electrons are free to move and are modeled as macroparticles.[12] These electrons move under the influence of the wave electric and magnetic fields (E_x, E_y, B_x, and B_y), an external applied magnetic field (B_z) and an electrostatic field produced by the ion and electron charges (E_z).

Particle loss and generation are not modeled, since in the 1D geometry used here, there is no reason to expect that the density profiles would evolve to those measured in the experiment. Thus, it would not be possible to correctly

simulate the effect of these measured densities. In addition, when ion motions are included, simulations typically reach steady state on time scales of the order of the mean ion transit time in the system, which is significantly longer than the time needed for the electrons and wave fields to reach a steady state. Thus, the simulation time would be increased by a few orders of magnitude. However, as will be seen in Sec. IV, the simulations reach a pseudo-steady-state after a time of about 0.1 μs, during which the ions would barely have moved, so that the assumption of immobile ions seems reasonable. Although only one spatial dimension is simulated, all three electron velocity dimensions are included (v_x, v_y, and v_z), so that the simulation is 1D3V.

III. NUMERICAL METHOD

As discussed above, EM waves are launched from the LHS boundary and allowed to propagate in the plasma. The EM fields are found from the Langdon–Dawson algorithm[12] (obtained from Maxwell's equations), which can be written as

$$\frac{1}{2}\left(\frac{\partial}{\partial t} \pm c\frac{\partial}{\partial z}\right)\left(E_x \pm cB_y\right) = \frac{d^{\pm}F}{dt} = -\frac{J_x}{2\varepsilon_0}, \tag{1}$$

where t and z are the temporal and spatial coordinates, c is the speed of light in vacuum, E_x and B_y are the wave electric and magnetic field components, respectively, J_x is the plasma current density, ε_0 is the permittivity of free space, and ${}^{\pm}F = 1/2(E_x \pm cB_y)$. The electric and magnetic field components are found from

$$E_x = {}^{+}F + {}^{-}F, \tag{2}$$

$$B_y = ({}^{+}F - {}^{-}F)/c. \tag{3}$$

Similar expressions to Eqs. (1)–(3) then exist for the wave components E_y and B_x, giving ${}^{\pm}G = 1/2(E_y \mp cB_x)$. The power or Poynting flux carried by each of the waves can be shown to be equal to[12]

$$S = \frac{1}{\mu_0 c}\left({}^{+}F^2 - {}^{-}F^2\right), \tag{4}$$

where μ_0 is the permeability of free space. Equation (1) can be written in a finite-difference form as

$$\frac{{}^{\pm}F(t+\Delta t, z \pm c\Delta t) - {}^{\pm}F(t,z)}{\Delta t} = -\frac{{}^{\pm}J_x(t+\Delta t/2, z \pm c\Delta t/2)}{2\varepsilon_0}, \tag{5}$$

where ${}^{\pm}J_x$ is a space and time centered average current density (see below). By then starting with known wave conditions at $z = -20$ cm (the LHS boundary) and $t = 0$, the wave components at any other position and future time can be determined from Eq. (5). It should be noted that Eq. (5) is only valid for $\Delta z = c\Delta t$, and thus a restriction is present on the spatial and temporal step sizes. The current densities used in Eq. (5) are obtained from

$${}^{\pm}J_x(t+\Delta t/2,\ z \pm c\Delta t/2) = \tfrac{1}{2}\left({}^{-}J_{x,j\mp1} + {}^{+}J_{x,j}\right), \tag{6}$$

where j represents the spatial grid number, and ${}^{-}J_x$ is found from the sum of the particle current densities using the velocities $v_x(t+\Delta t/2)$ linearly weighted to the grid using the particle positions at $z(t)$, while ${}^{+}J_x$ is found from the sum of particle current densities using the velocities $v_x(t+\Delta t/2)$ linearly weighted to the grid using the particle positions at $z(t+\Delta t)$. This can be expressed mathematically as

$${}^{+}J_{x,j}^{n+1/2} = \sum_i q_i v_{x,i}^{n+1/2} S\left(Z_j - z_i^{n+1}\right), \tag{7}$$

$${}^{-}J_{x,j\mp1}^{n+1/2} = \sum_i q_i v_{x,i}^{n+1/2} S\left(Z_{j\mp1} - z_i^{n}\right), \tag{8}$$

where i represents the particle number, q_i is the particle charge, S is a shape factor describing the particle shape (and thus defining the interpolation scheme, which is linear here), Z_j is the position of the jth grid point, and the superscript n defines the time step number. A similar expression then exists for the current densities J_y. At the left-hand boundary, RHP EM waves enter the system, while the right-hand side is treated as an "open" boundary. This boundary is not strictly speaking open, since it represents a plasma/vacuum interface, and waves suffer almost complete reflection here. The boundary conditions can be stated explicitly as

$${}^{+}F(z = -20\text{ cm},\ t) = E_0 \cos \omega t, \tag{9}$$

$${}^{+}G(z = -20\text{ cm},\ t) = E_0 \sin \omega t, \tag{10}$$

at the LHS, while at the RHS, we have

$${}^{-}F(z = -25\text{ cm},\ t) = 0, \tag{11}$$

$${}^{-}G(z = -25\text{ cm},\ t) = 0. \tag{12}$$

Since, under the conditions to be simulated, the plasma has a dielectric constant of the order of 100, the EM wave (which is launched from vacuum) initially suffers a large upstream reflection, and only a small transmitted wave actually enters the plasma. The initial wave amplitude, E_0, is chosen so that this transmitted wave has an amplitude estimated to be present in the experiment (which is of the order of 100 V m^{-1}, thus requiring $E_0 = 10\,000$ V m^{-1}). Due to numerical noise, an artificial instability was observed if the right-hand boundary is completely reflecting [i.e., ${}^{-}F(z = -25\text{ cm},\ t) = -{}^{+}F(z = -25\text{ cm},\ t)$].

The above equations have focussed on determining the EM wave properties, but in order for the plasma particles to communicate with each other due to their own electric charge, additional electric fields are needed. Since the system is 1D, this electrostatic field acts in the z direction only. In most other PIC simulations, this electrostatic field is found from a solution of Poisson's equation, using specified boundary conditions. In the present case, since particle loss is not modeled, we assume that there is no net charge at each of the boundaries. Under these conditions then, the total charge in the system is known, and thus the electric field can be found directly from Gauss's law. In 1D, Gauss's law takes the form

$$\frac{dE_z}{dz} = \frac{\rho}{\varepsilon_0}. \tag{13}$$

By then discretizing Eq. (13) and integrating from one spatial grid point to the next (using the trapezoidal rule), the electric field is obtained as

$$E_{z,j+1} - E_{z,j} = \frac{\rho_{j+1} - \rho_j}{2\varepsilon_0}\Delta z. \tag{14}$$

Here E_z and ρ are the electric field and charge density at each of the grid points labeled j and $j+1$. The charge density is also obtained using linear weighting to the grid and can be given by

$$\rho_j = \sum_i q_i S(Z_j - z_i)\,. \tag{15}$$

Only one boundary condition is needed for Eq. (14), which is the electric field at the LHS boundary, and by assuming zero net charge at this location, $E_{z,0} = 0$. Note, however, that use of Eq. (14) requires that the charge density both within the plasma and on the boundary walls be known. In general, this is not the case, since only the potential is known on the boundaries. In these cases, Poisson's equation must then be solved instead.[12]

About 4×10^5 electrons are used, loaded with a Maxwellian distribution and a temperature of 6 eV (matching that of previous measurements[8]). To minimize initial noise levels, the electrons are loaded in phase space using a quiet start algorithm based on bit-reversed numbers.[12] The external magnetic fields in Fig. 2(a) are loaded into the simulation, and electrons are moved using a leap-frog scheme applied to the relevant equations of motion, which gives the following finite difference equations:

$$\frac{\boldsymbol{v}_{t+\Delta t/2} - \boldsymbol{v}_{t-\Delta t/2}}{\Delta t} = \frac{q}{m}\left(\boldsymbol{E} + \frac{\boldsymbol{v}_{t+\Delta t/2} - \boldsymbol{v}_{t-\Delta t/2}}{2} \times \boldsymbol{B}\right), \tag{16}$$

$$\frac{\boldsymbol{r}_{t+\Delta t} - \boldsymbol{r}_t}{\Delta t} = \boldsymbol{v}_{t+\Delta t/2}, \tag{17}$$

where q and m are the electron charge and mass, respectively. Here, the electric and magnetic fields, $\boldsymbol{E}$ and $\boldsymbol{B}$, and particle positions, $\boldsymbol{r}$, are known at integral times (t, $t+\Delta t$, $t+2\Delta t$, …), while the particle velocities, $\boldsymbol{v}$, are known at half integral times ($t-\Delta t/2$, $t+\Delta t/2$,…). Equation (16) is then integrated using the algorithm of Boris,[12] which isolates the electric and magnetic forces, allowing the acceleration due to the electric field and the rotation due to the magnetic field to be calculated separately. Electron-neutral collisions are included in some runs of the simulation using a standard Monte Carlo collision algorithm.[13] Energy loss from excitation and ionization still occur, but particle creation during an ionization event is not modeled.

Since the maximum plasma densities simulated are around $1 - 2 \times 10^{17}$ m^{-3}, in order to maintain numerical stability and restrict numerical heating,[12] the Debye length needs to be resolved, thus requiring about $1.5 - 2 \times 10^4$ grid points for the self-consistent electrostatic field. Since the current densities need not resolve the Debye length, a coarser mesh is used with about 500 grid points. As described above, Eq. (5) requires $\Delta t = \Delta z/c$, and this then sets $\Delta t = 3 \times 10^{-12}$ s (due to the number of grid points chosen). This time step also automatically satisfies the additional PIC stability criterion, $\Delta t < 0.2/\omega_{pe}$,[12] where $\omega_{pe} = (q^2 n_0/\varepsilon_0 m)^{1/2}$ is the electron plasma frequency, with n_0 the plasma density. Tests with the wave excitation off were done to check for numerical heating, which was found to be small (only a few percent) after a time equal to the total simulation time to be used.

IV. RESULTS

A. Code validation

Before running the PIC code to simulate the *Piglet* system, a number of test runs were performed to check that it correctly reproduced the dispersion relation for helicon waves. In these tests, a constant plasma density and magnetic field were loaded, together with cold electrons (this also allowed fewer particles to be needed for these tests). The resulting wavelength was then determined and compared with that expected from helicon theory. For EM waves traveling in an infinite, uniform plasma, the dispersion relation (accounting for finite electron mass) can be given by[1]

$$\frac{k^2 c^2}{\omega^2} = \frac{\omega_{pe}^2}{\omega(\omega_{ce}\cos\theta - \omega)}, \tag{18}$$

where k is the wave number, ω is the wave angular frequency, θ is the angle between the wave vector and the applied magnetic field, and $\omega_{ce} = qB_0/m$ is the electron cyclotron frequency. A number of simulations were then run with varying applied magnetic fields (B_0), plasma densities (n_0), and excitation frequencies ($\omega = 2\pi f$), with the results shown in Fig. 3 [since we are dealing with parallel propagation here, $\theta = 0$ in Eq. (18), and so $k = k_z = 2\pi/\lambda_z$, with λ_z the wavelength]. Here the simulation results are in good agreement with helicon theory over the whole range of values investigated. In addition, standing wave behavior is observed (as expected) due to wave reflection that occurs at the RHS boundary. These results demonstrate that the PIC code is capable of correctly simulating EM wave propagation.

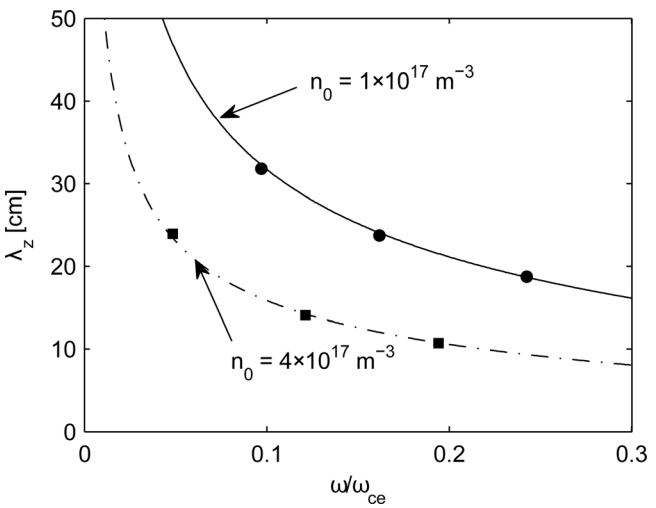

FIG. 3. Helicon wavelength, λ_z, as a function of the normalized frequency, ω/ω_{ce}. The solid and dashed lines show the results from helicon theory [Eq. (18)], while the closed circles and squares show the wavelengths found from the PIC simulations.

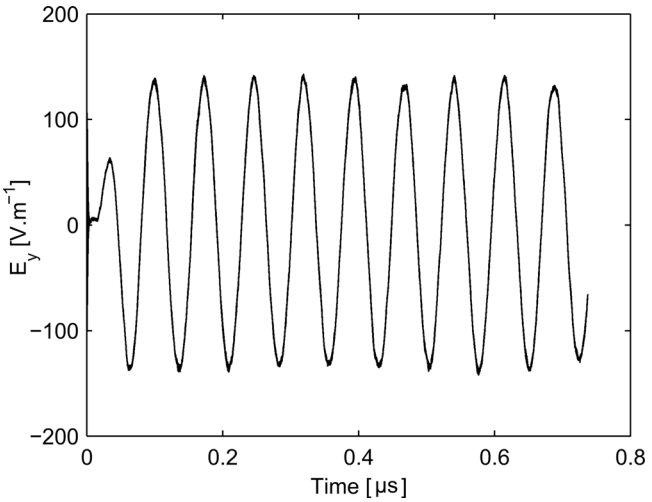

FIG. 4. Wave electric field (E_y) at $z = -11$ cm as a function of time for magnetic field test case A in Fig. 2(a). After an initial transient period, the electric field reaches a definite steady state at about 0.1 μs.

B. Wave propagation in a diverging magnetic field

With electron-neutral collisions off, and beginning with the most important test case [test case A in Fig. 2(a)], after an initial transient period, the simulation was observed to reach a pseudo-steady-state after about 0.1 μs. Since, as discussed in Sec. II, particle loss and creation are not modeled, the system cannot produce a self-consistent density profile, and so a true steady state is never reached. However a pseudo-steady-state does occur once the wave behavior does not change on time scales greater than an rf period. This pseudo-steady-state is illustrated in Fig. 4, which shows the wave electric field component, E_y, plotted as a function of time. Here the wave amplitude is seen to settle to a roughly constant value at about 0.1 μs. After this time was reached, as a check, the simulation was run for a further 9 rf periods. As is seen in the figure, the wave behavior remains similar for each of these extra rf periods. The frequency of the simulated wave in Fig. 4 is equal to 13.56 MHz, which matches that of the excitation frequency used at the LHS boundary.

After the total simulation time (0.74 μs) has been run, the electron density is averaged over an rf period to investigate whether the electrostatic field (E_z) correctly acts to confine the electrons to the loaded background ion density profile. This is shown in Fig. 5, where the black closed circles (representing the electron densities at the grid points; for clarity, not all of the grid points are shown), are seen to match very well with those of the background ions, thus showing that the electrostatic field correctly functions to constrain the elections during the simulation.

Plots of the wave electric and magnetic fields, together with the electron current densities, are shown in Figs. 6(a)–6(c) after the total simulation time (≈0.8 μs). As seen, the wave amplitude is roughly constant at about 150 V m^{-1} and 70 μT for the electric and magnetic field components, respectively, for $z < -8$ cm, before rapidly decaying to almost zero in the region -8 cm $< z < 2$ cm. The current density observed in the

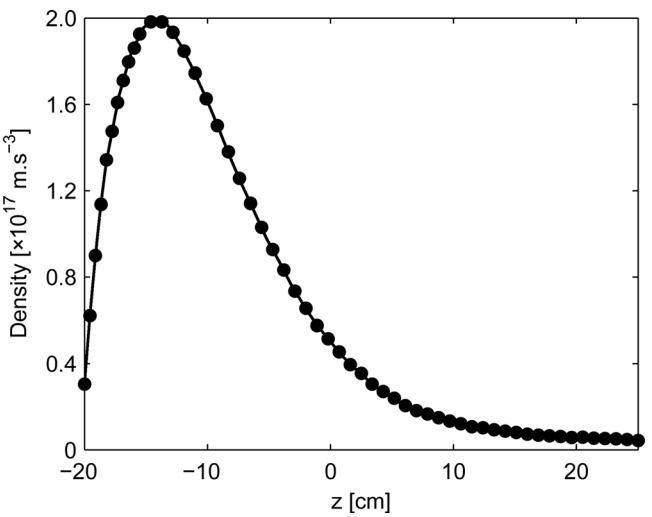

FIG. 5. Ion- (solid line) and time-averaged electron (black closed dots; averaged over an rf period) densities as a function of axial distance after a simulation time of around 0.74 μs.

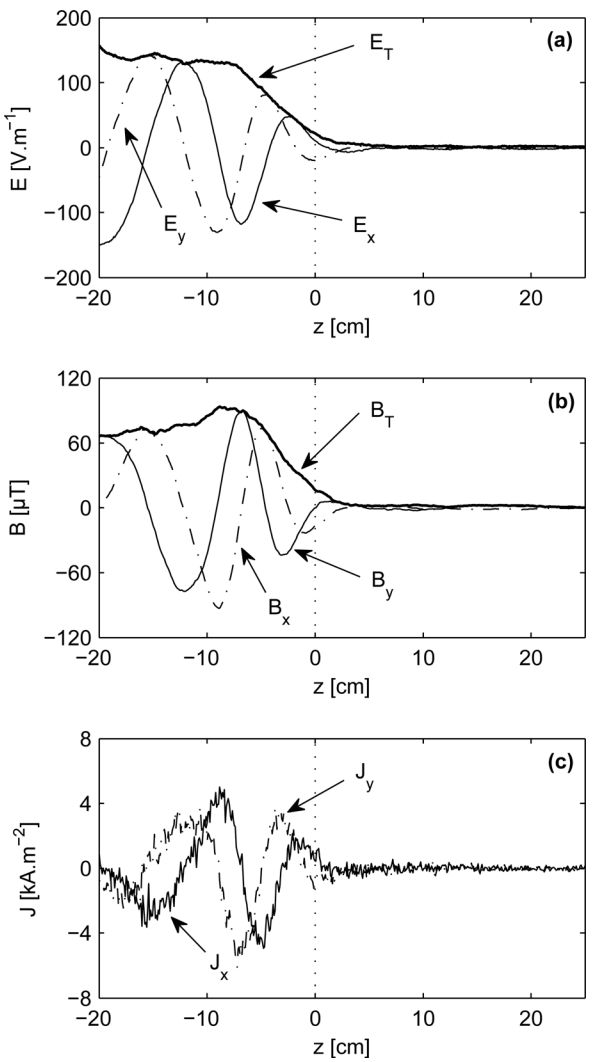

FIG. 6. (a) Wave electric field, (b) wave magnetic field, and (c) electron current densities from the PIC simulation for magnetic field test case *A* in Fig. 2(a). E_T and B_T are the total amplitude of the right-hand polarized helicon wave given by $E_T = \sqrt{E_x^2 + E_y^2}$ and $B_T = \sqrt{B_x^2 + B_y^2}$, respectively. The vertical dotted lines show the location of the source tube exit in *Piglet*.

downstream region ($z > 2$ cm) is virtually zero, consistent with the absence of an electric field in this region. Observation of the total electric and magnetic field amplitudes (bold solid lines) shows no standing wave patterns (which would manifest as distinct peaks). In addition, by observing the spatiotemporal behavior of the wave (which will be discussed in Sec. IV E below), the wave appears to be traveling, with no standing wave structures present. This implies that little or no wave reflection occurs in the region $-8 < z < 0$ cm and, thus, that the wave is being absorbed.

C. Electron–cyclotron damping

The results in Sec. IV B suggest that the incident wave is a traveling wave within the plasma, and since it is not seen in the downstream region ($z > 0$ cm), wave absorption must therefore take place close to the source tube exit. Figure 7(a) shows the time-averaged (over one rf period) power flux of the EM waves, found using Eq. (4). The two wave components $(E_x - B_y)$ and $(E_y - B_x)$ contribute near identical power fluxes (as expected), with each showing a roughly constant power flux of about 4 kW m^{-2} for $z < -9$ cm. A peak in the flux is then seen for $-9 < z < -6$ cm (discussed below), before it rapidly decays to zero for $z > -6$ cm and remains so throughout the diffusion chamber ($z > 0$ cm). The total RHP wave flux is given by the bold solid line, which is the sum of the fluxes of each of the wave components. The total wave power that enters at the LHS boundary is seen to be about 8.1 kW·m^{-2}, while the total power that leaves the RHS boundary is 0 kW·m^{-1}. Since no standing waves or wave reflection seem to occur, this suggests that the total input power must be being absorbed.

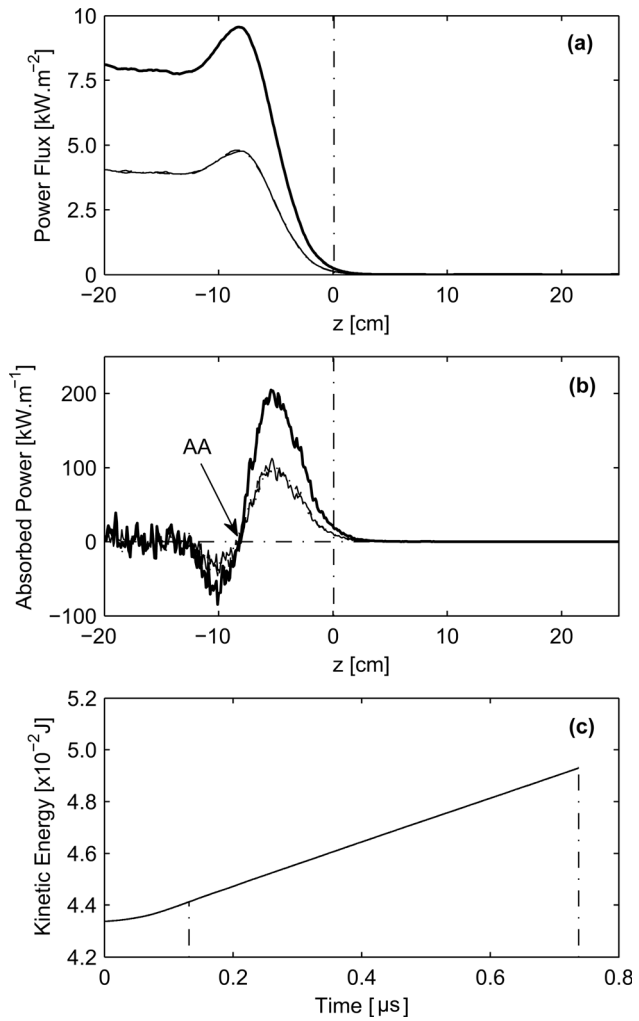

FIG. 7. (a) Spatial profile of the time-averaged power flux of the RHP wave (bold solid line) and each of the individual wave components, $E_x - B_y$ (light solid line) and $E_y - B_x$ (light dashed line). (b) Spatial profile of the absorbed power per unit length of the RHP wave (bold solid line) and each of the individual wave components, $E_x - B_y$ (light solid line) and $E_y - B_x$ (light dashed line). (c) Total electron kinetic energy as a function of simulation time. Between the two vertical dashed lines, the simulation has reached a pseudo-steady-state and the kinetic energy increases linearly. The vertical dotted lines in (a) and (b) show the location of the source tube exit in *Piglet*.

The peak in the power flux that occurs at about $z = -8$ cm in Fig. 7(a) is at first peculiar, since it is unexpected that the wave power should increase, especially since there does not appear to be a power source available for this to occur. However, certain electrons heated within the cyclotron resonance zone can stream to this location (due to their axial velocity, v_z), and if their phase is correct, power can be transferred to the wave. That is, negative power transfer occurs, as has been experimentally observed in inductive sources[14] and theoretically predicted.[15] The time-averaged (over one rf period) power absorbed by the plasma per unit axial length, $\langle P_{\text{abs}} \rangle_L$, can be found from the work-energy theorem of electrodynamics and, in particular, can be given by[11]

$$\langle P_{\text{abs}} \rangle_L = \frac{1}{T} \int_0^T \int_A \boldsymbol{E}(z,\, t) \cdot \boldsymbol{J}(z,\, t)\, dA dt, \tag{19}$$

where A is the cross-sectional area of the simulation, T is an rf period, and $\boldsymbol{E}$ and $\boldsymbol{J}$ are the wave electric field and electron current densities, respectively. This absorbed power is shown in Fig. 7(b). Here it is seen that the absorbed power is approximately zero for $z < -11$ cm, as well as for $z > 0$ cm, but there is a large broad peak between about $-8 < z < 0$ cm and a smaller negative peak between $-12 < z < -8$ cm. This smaller peak corresponds to the negative power transfer from the particles to the wave, while the larger positive peak corresponds to power absorption of the wave by the electrons. By integrating the power absorbed per unit length [Eq. (19)] over the whole simulation length, the net absorbed power is obtained as 8 kW·m^{-2}, which is equal to the total wave power that enters the simulation. This thus says that the electrons do indeed absorb all of the wave power.

As a final check, if the electrons are indeed accounting for all of the power absorption, then once the pseudo-steady-state has been reached, since a constant wave power enters the system, the electron energy should increase linearly with time, and this rate of increase should equal the power input. Figure 7(c) shows the total electron kinetic energy as a function of simulation time. After about $0.1 - 0.15$ μs, close to the time needed to reach the pseudo-steady-state (see Fig. 4), the rate of increase of electron energy is indeed linear. By taking the gradient of this line [in the region between the two vertical dashed lines in Fig. 7(c)], the slope is found as 8.5 kW·m^{-2}, very close to the total absorbed power and total

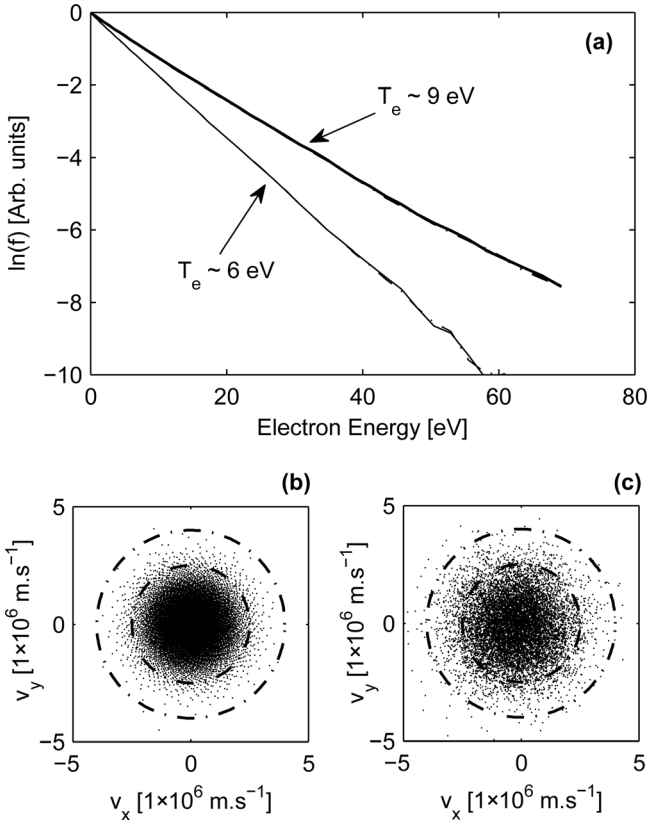

FIG. 8. (a) Distribution function, f, for electrons within the absorption zone ($-8 < z < 0$ cm), with f_x (solid line) and f_y (dashed line). The light solid and dashed lines show the distribution functions at $t = 0$ s, while the bold solid and dashed lines show the distribution functions at $t = 0.74$ μs. (b) Electron phase space between $z = -4$ cm and $z = -3$ cm at $t = 0$ μs. (c) Electron phase space between $z = -4$ cm and $z = -3$ cm at $t = 0.81$ μs. The dashed circles in (b) and (c) serve as a visualization aid.

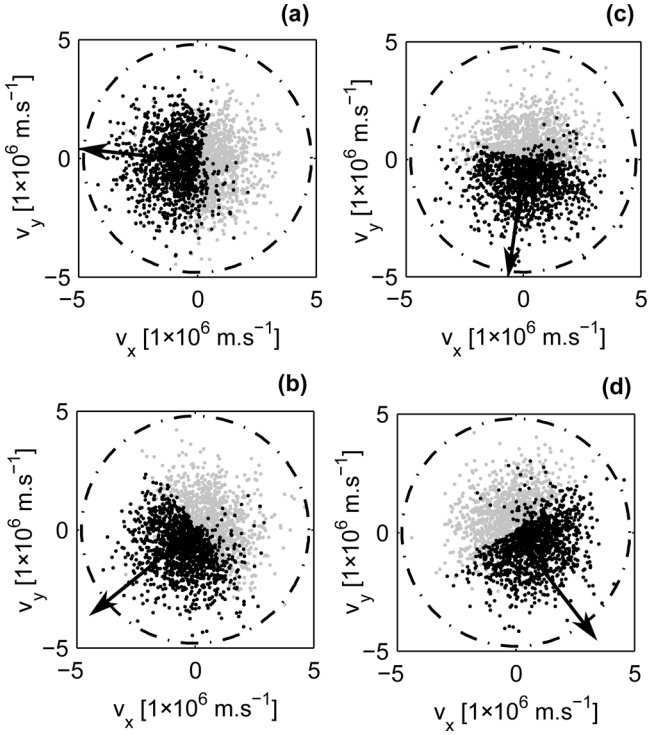

FIG. 9. Electron phase space between $-4.1 < z < -3.9$ cm after 0.74 μs and at an rf phase of (a) 0°, (b) 45°, (c) 90°, and (d) 135°. The black dots represent electrons that gain a net energy during each rf phase interval in (a)–(d). The bold arrows indicate the negative of the direction of the electric field vector ($-\boldsymbol{E}$) at $z = -4$ cm at each rf phase. The dashed circles in (a)–(d) serve as a visualization aid.

input power. The slight difference can be attributed to the small numerical heating, which was discussed in Sec. III.

While the total electron kinetic energy was observed to increase within the simulation, observation of the electron distribution function should directly show the effect of electron heating. Figure 8 shows the electron energy distribution function for the x (solid line) and y (dashed line) directions at $t = 0$ μs (light lines; averaged over an rf period) and after $t = 0.74$ μs (bold lines; averaged over an rf period) for electrons within the absorption zone ($-8 < z < 0$ cm). The electrons begin with a temperature of about 6 eV (which is the temperature the particles were initially loaded with), but after about 10 rf periods, the electron temperature has risen to about 9 eV. The temperature of the distribution in the z direction (not shown), however, still remains between 5 and 6 eV. This electron heating can be seen further by plotting the electron phase space at $t = 0$ μs, as in Fig. 8(b), and at $t = 0.74$ μs, as in Fig. 8(c). The dashed circles in these figures serve as a visualization aid. Observation of Fig. 8(b) shows that there are very few electrons present outside of the outer circles, while Fig. 8(c) shows a far greater number. In addition, the number of electrons between the two circles in Fig. 8(c) has increased.

While we have shown above that the electrons appear to absorb the wave power, we have not demonstrated yet that this is due to cyclotron damping. This can be shown explicitly by observing phase space acceleration for electrons within the absorption zone, as in Fig. 9. This plot shows electrons located between $-4.1 < z < -3.9$ cm (at approximately the location of the maximum absorbed power) at each of the rf phases specified in the figure caption. The black dots represent electrons whose energy increases between each of the rf phase intervals (since the electrons have a parallel velocity, they very quickly move away from the region $z \approx -4$ cm, so that only a small time interval can be used to observe acceleration directly). The dashed circles serves as a visualization aid, while the bold black arrow represents the negative of the wave electric field vector at $z = -4$ cm at each rf phase. As the rf phase changes, the energy of the black electrons increases between each interval, and this is strongly correlated with the rotation of the electric field vector, showing the acceleration is performed by this field. In fact, the electric field vector is seen to accelerate approximately all electrons located in the upper half plane of a coordinate system where the electric field vector defines the y-axis (and which rotates with changing rf phase). In addition, the total net energy of all the electrons increases for each rf phase (hence, the electrons are heated with time). Note that since the electrons have a negative charge, it is the negative of the electric field that provides the acceleration.

D. Parametric investigation

In order to confirm electron–cyclotron damping as the mechanism responsible for the wave absorption, a number of

further simulations are performed so as to check that the correct parametric dependence is present. Cyclotron damping is a kinetic phenomenon, and as a guide, parametric dependencies can be obtained from the dispersion relation for waves in a warm plasma, which is given by[16]

$$1 - \frac{k_z^2 c^2}{\omega^2} + \frac{\omega_{pe}^2}{\omega k_z v_t} Z(\xi) = 0, \tag{20}$$

where the wave number is complex, $k_z = k_r + ik_i$, $v_t = \sqrt{2qT_e/m}$ is the mean electron speed, $\xi = (\omega - \omega_{ce} + iv)/k_z v_t$, v is the electron collision frequency, and $Z(\xi)$ is the plasma dispersion function. In Eq. (20), the ions are assumed to be immobile, the electrons have a Maxwellian distribution, and the plasma density and external magnetic field are uniform. Because of cyclotron damping, the wave number is complex, with the term representing damping given by k_i. For a given electron temperature, T_e, plasma density n_0 (which manifests itself through the plasma frequency, ω_{pe}), and excitation frequency, f, Eq. (20) can be solved for the wave number as a function of the normalized frequency, ω/ω_{ce}. By defining the onset of cyclotron damping at the point where $k_i = 1\ \mathrm{m}^{-1}$, the normalized damping onset frequency, $[\omega/\omega_{ce}]_{onset}$, can then be determined.

A number of additional PIC simulations are then run, where we set the plasma density to a constant value and make use of magnetic field configuration A in Fig. 2(a). By then varying the electron temperature, plasma density, excitation frequency, and magnetic field amplitude (but still keeping the same magnetic field shape), the normalized onset frequency can be found from the simulation, by using the magnetic field that is located at the point where damping first begins [point AA in Fig. 7(b)]. These results are then plotted in Fig. 10 together with the results from Eq. (20). Here the standard parameters chosen are $T_e = 6$ eV, $n_0 = 2 \times 10^{17}\ \mathrm{m}^{-3}$, $f = 13.56$ MHz, and the maximum magnetic field is $B_0 = 4$ mT, while Fig. 10(a) shows results for varying temperature, Fig. 10(b) shows results for varying densities, and Fig. 10(c) shows the results for varying excitation frequency. As is seen, for all of the parameters, the simulation shows the same general trends as that exhibited by Eq. (20) and, in addition, show a fairly good quantitative agreement, in spite of the nonuniform magnetic field profile used. If the magnetic field amplitude is changed, then the damping onset point is observed to move within the simulation, approximately occurring at the same magnetic field strength for each amplitude. These results all provide further evidence to confirm the hypothesis of cyclotron damping as found in Sec. IV C.

E. Observation of wave trapping

Before the results for the other magnetic field tests cases in Fig. 2(a) are presented, some experimental results from Ref. 8 are repeated here and presented in a different form. In Ref. 8, B_z wave fields were measured in the axial direction in the downstream region with a B-dot probe [located at $r = 4.8$ cm; see Fig. 1(a)], and profiles of the wave amplitude and phase were presented. Here, we make use of a spatiotemporal

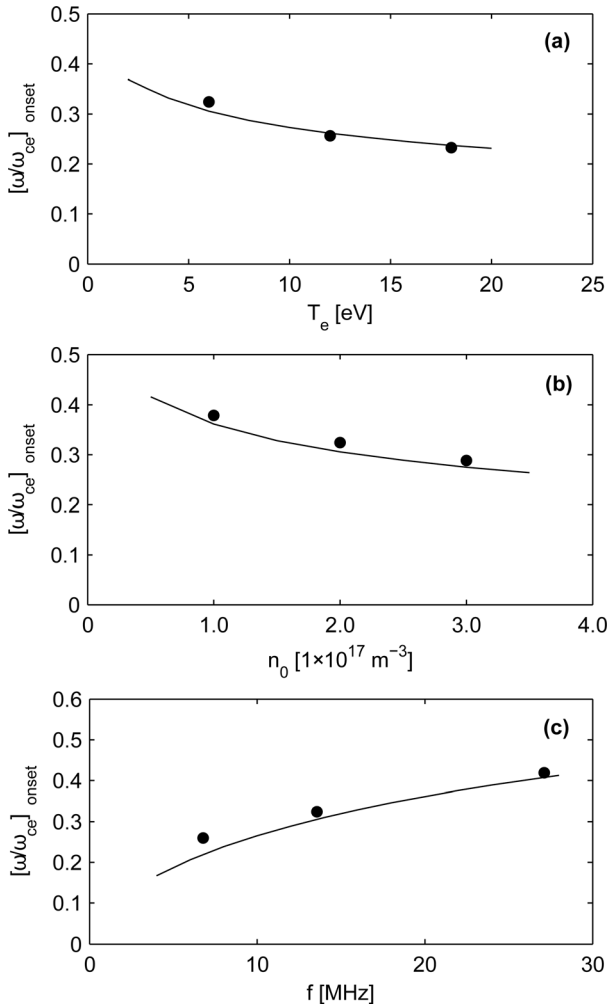

FIG. 10. Normalized wave damping onset frequency, $[\omega/\omega_{ce}]_{onset}$, as a function of (a) electron temperature (T_e), (b) plasma density (n_0), and (c) wave excitation frequency (f). The solid lines show the theoretically expected onset frequency found from Eq. (20), while the closed black circles show the onset frequency found from the simulations.

plot produced from these measured wave amplitudes, $B_{z_0}(z)$, and phases, $\theta(z)$, together with the equation

$$B_z(z, t) = B_{z_0}(z)\ \sin\left[\omega t + \theta(z) + \phi\right], \tag{21}$$

where ω is the angular frequency of the wave, t is a time variable, and ϕ is an arbitrary phase constant. By then plotting this for ωt from 0 to 2π, Fig. 11 is generated. Note that as discussed in Ref. 8, standing wave behavior is observed in the source region, which appears related to the near fields of the antenna and not to the helicon waves. For case A, the wave magnitude in the downstream region is small, and traveling wave behavior is not seen. As the magnetic field is increased, however, traveling wave behavior becomes evident (candy-stripe pattern for $z > 0$ cm for cases B and C in Fig. 11), and the wave magnitude begins to increase in the downstream region. Finally, for case D, a standing wave pattern begins to develop, indicating that waves have reached the back plate of the diffusion chamber (where they can undergo reflection).

The additional magnetic field test cases (B–D) in Fig. 2(a) are then simulated, and together with case A, spatiotemporal

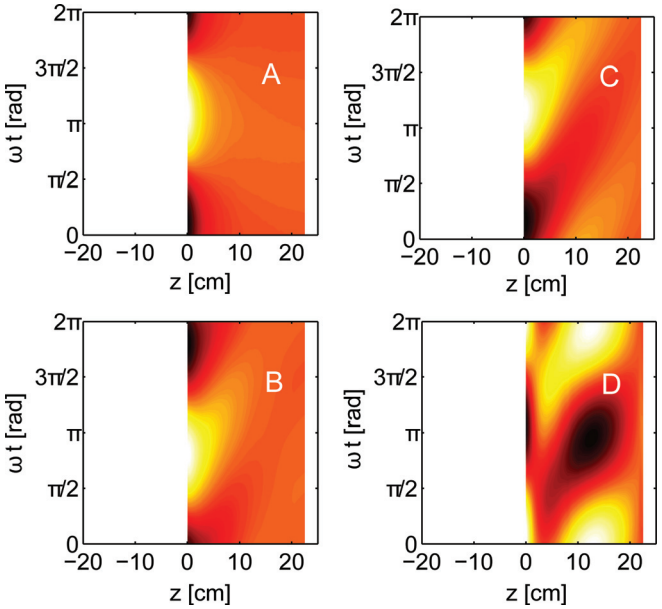

FIG. 11. (Color online) Experimental measurements of the B_z component of the helicon wave in the diffusion chamber taken with the B-dot probe (at $r = 4.8$ cm) and making use of Eq. (21), for the magnetic field test cases in Fig. 2(a). The plots are normalized such that the light regions correspond to 1, and the dark regions to −1.

plots of the wave electric field, E_y, are produced after a total simulation time of about 0.8 μs, as shown in Fig. 12. For case A, a candy-stripe pattern is seen, indicating traveling wave behavior, with the wave amplitude decreasing near $z = 0$ cm. In the downstream region ($z > 0$ cm), no waves are observed at any point in the rf cycle, consistent with the experimental results in Fig. 11 for this case. As the magnetic field is changed according to Fig. 2(a), however, traveling waves are seen in the downstream region, which eventually transition to a standing wave pattern (cases C and D) as waves are able to reach the RHS boundary (where they can suffer reflection). This is again consistent with the experimental results in Fig. 11 and suggests that the simulation has captured the essential physics within the experiment. While the results in Fig. 12 were obtained using the loaded densities shown in Fig. 2(b), densities half as large were also simulated, with similar results obtained.

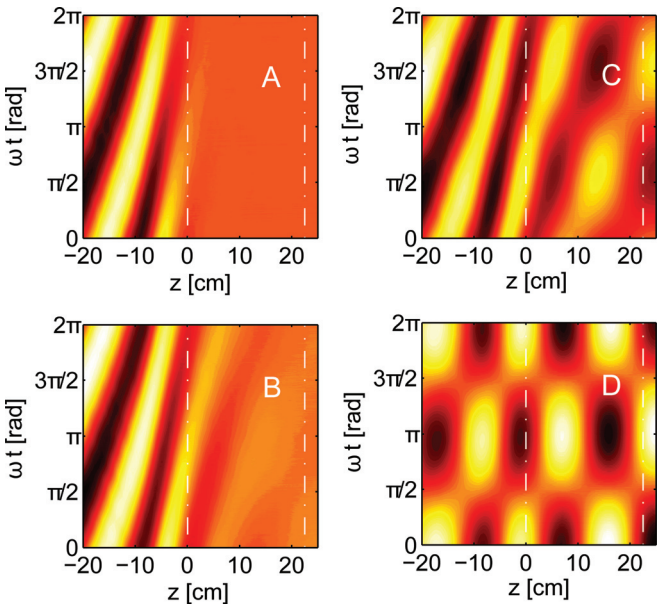

FIG. 12. (Color online) Spatiotemporal evolution of the E_y component of the helicon wave from the PIC simulations, for the magnetic field test cases in Fig. 2(a). The white vertical dashed lines show the region in the simulation corresponding to the diffusion chamber in *Piglet* where the experimental measurements in Fig. 11 were taken. The plots are normalized such that the light regions correspond to 1, and the dark regions to −1.

V. DISCUSSION

As mentioned, based on previous experimental observations, helicon waves were observed in the upstream source region of *Piglet* but were absent in the downstream chamber. As the magnetic field was changed slightly, however, waves could be made to "escape" the source region and were then able to propagate freely downstream. At the time, it was unclear whether waves were being absorbed or reflected near the source exit, and while such a question might be answered experimentally, this was complicated by the presence of the rf antenna. B-dot probe measurements in this region shown there to be a standing wave behavior under the antenna, which was present even with the plasma off. Further tests showed that this behavior could be correlated with the shape and structure of the antenna, and thus the near fields of the antenna appeared to be obscuring the true wave fields. Thus, direct observation of wave reflection or absorption would be difficult and possibly questionable.

It is for the above reasons that a PIC simulation was written, so as to try and reproduce the observed behavior and gain insight into whether reflection or absorption would occur. The simulations presented in Sec. IV have successfully reproduced some of the observed experimental results and show that no significant wave reflection occurs. Indeed, cyclotron damping appears strong enough in the initial configuration [case A in Fig. 2(a)] to completely "stop" the wave before it reaches the downstream region. Direct phase space acceleration and electron heating was observed, and the simulation results show the correct parametric dependencies, indicating that cyclotron damping is the likely cause of the wave absorption. As the magnetic field is changed [case B–D in Fig. 2(a)], the damping decreases, and the waves can make it downstream. These simulation results are consistent with experiment and seem to provide a feasible explanation for the previously observed phenomenon.

In the simulations above, since no energy loss mechanism exists for the electrons, we might imagine that either their energy increases unbounded or that, after a very large amount of time, a "new" steady state is reached where instead of absorption, wave reflection must occur.[15] Within the simulations, such situations can only arise if the energy of the electrons increases to such an extent that Doppler-shifting effects would require cyclotron damping to occur for magnetic field strengths no longer present within the simulation region. This situation is unphysical, since it means the electrons would have a very large temperature. A combination of electron-neutral collisions and electron loss at system boundaries within the experiment prohibits such a situation from occurring.

Nevertheless though, for completeness, if electron-neutral collisions are activated in the simulations [for a pressure of 0.08 Pa (Ref. 8)], similar behavior to Figs. 6 and 12 is still observed, so that the collisionless results seem representative of what would occur in the experiment.

Due to the 1D nature of the simulations, however, higher-dimensional effects associated with the *Piglet* reactor and helicon waves cannot be ruled out. The wave damping appears slightly larger in the experiment than the simulation, since, for case C in the experiment, standing wave behavior has not yet set in. This seems most likely a consequence of the 1D nature of the simulations. In the experiment, as the waves enter the downstream chamber, they can undergo expansion so that the wave amplitude would decrease. Moreover, since the waves in the simulation are not radially bounded, no parallel (E_z) wave components are present. This means that the axial wavelength in the simulation will be slightly different from the experiment (as is indeed seen by comparing Figs. 11 and 12), and also that any possible wave-particle trapping in the parallel electric field of the helicon wave[17,18] cannot occur. In addition, helicon wave absorption is known to strongly depend on the radial boundary conditions.[19,20] In a radially bounded system, where waves need not propagate parallel to the applied magnetic field, the dispersion relation in Eq. (18) need not have $\theta = 0$, and now for a given density, magnetic field, and axial wave number (k_z), two solutions for the perpendicular wave number ($k_\perp$) exist, known as the helicon and Trivelpiece-Gould (TG) modes, respectively. The radial boundary can lead to mode coupling between these two waves, which can enhance the absorption process. Indeed, for low-field helicons, Cho[7] has shown that the plasma resistance can be large when the helicon and TG waves merge, suggesting mode coupling as an important mechanism in this regime. In the PIC simulations (which are 1D), any mode coupling and radial boundary effects cannot be simulated, so the impact of these factors is difficult to assess. The experimental results under the magnetic field test cases in Fig. 2(a) (Ref. 8) demonstrate that the effect of the magnetic field near the source exit clearly has a significant effect on the subsequent wave and plasma properties, even though the magnetic field within the source region is similar. Previous numerical studies,[6,7] however, cannot self-consistently account for cyclotron damping, nor can they accommodate diverging magnetic fields as used here. It is thus unclear what effect (if any) changes to the applied magnetic field profile [such as those in Fig. 2(a)] would have on any mode coupling effects.

Additional considerations worth discussing are the results of Olson.[21] Olson has performed a detailed kinetic analysis of spatial cyclotron damping in an infinite uniform plasma, immersed in a uniform magnetic field, directly treating the excitation of waves from a simple source. The plasma response to this excitation is found to consist of a number of terms, with the cyclotron-damped term being dominant for $z > 1 \approx c/\omega_{ce}$ as long as $(\omega_{pe}/\omega_{ce})^2(c/v_t) \ll 1$. If this length criterion is not met, then additional plasma response terms are still significant. For representative plasma parameters in the current investigation, we have $l \sim 1$ m and $(\omega_{pe}/\omega_{ce})^2\ (c/v_t) \sim 1 \times 10^6 \gg 1$, and thus to successfully measure cyclotron damping, measurements would need to be made at distances of about 1 m away from the antenna, which we note is more than twice the length of the entire reactor. It is uncertain, however, how this criterion would change in the presence of a nonuniform magnetic field, since it seems quite clear that even if cyclotron damping is not the only dominant term present, if it is strong enough, any wave will be damped well before a length of 1 m. It is also unclear how this criterion would change if radial boundary conditions were accounted for, since the wavelength of the helicon waves here is of a similar dimension to that of the radial source tube diameter. Nevertheless, this argument does highlight the fact that further direct quantitative measurements of cyclotron damping within the experimental reactor might be complicated or, in fact, impossible to perform.

Finally, it is worth briefly discussing the apparent negative power transfer observed in the simulations in Fig. 7. Negative power transfers have been predicted theoretically[15] and have previously been observed experimentally in inductive plasma reactors.[14] In the present case, it seems as if certain electrons heated in the absorption zone, due to their parallel velocity, can free-stream to other locations in the system, and if they have the correct phase, they can now transfer power to the wave itself. This feature was an unexpected outcome of the simulations and was not initially studied in the experiments, nor has it been investigated further. Future experimental work might be able to observe this effect directly, although the presence of the antenna itself, and the considerations of Olson, might make this difficult.

VI. CONCLUSIONS

In summary, we have performed 1D PIC simulations of helicon waves in low diverging magnetic fields. The results are consistent with experimental measurements and provide strong evidence to suggest that helicon wave trapping previously observed should be attributed to electron–cyclotron damping in the spatially decaying magnetic field. The simulations show that in the original magnetic field configuration, cyclotron damping is sufficiently strong to cause complete absorption of the helicon wave, and as a result, it is not able to propagate downstream. As the magnetic field is changed slightly, however, cyclotron damping decreases and the waves are able to propagate freely into the downstream region. The cyclotron damping process displays the correct parameter dependencies expected, and the simulations show that the uniform warm plasma dispersion relation gives a reasonable indication of where damping begins even in the presence of nonuniformities in the magnetic field.

[1]R. W Boswell and F. F. Chen, IEEE Trans. Plasma Sci. **25**, 1229 (1997).
[2]F. F. Chen, J. Vac. Sci. Technol. A **10**, 1389 (1992).
[3]G. Sato, W. Oohara, and R. Hatakeyama, Plasma Sources Sci. Technol. **16**, 734 (2007).
[4]S. J. Wang, J. G. Kwak, C. B. Kim, and S. K. Kim, Phys. Lett. A **313**, 278 (2003).
[5]T. Lafleur, C. Charles, and R. W. Boswell, Phys. Plasmas **17**, 043505 (2010).
[6]F. F. Chen, Phys. Plasmas **10**, 2586 (2003).
[7]S. Cho, Phys. Plasmas **13**, 033504 (2006).
[8]T. Lafleur, C. Charles, and R. W. Boswell, Phys. Plasmas **17**, 073508 (2010).

[9]B. McVey and J. Scharer, Phys. Rev. Lett. **31**, 14 (1973).
[10]C. Christopoulos, R. W. Boswell, and P. J. Christiansen, Phys. Lett. **47A**, 239 (1974).
[11]M. A. Lieberman and A. J. Lichtenberg, *Principles of Plasma Discharges and Materials Processing* (John Wiley & Sons, New Jersey, 2005).
[12]C. K. Birdsall and A. B. Langdon, *Plasma Physics Via Computer Simulation* (McGraw-Hill, New York, 1985).
[13]V. Vahedi and M. Surendra, Comput. Phys. Commun. **87**, 179 (1995).
[14]V. A. Godyak and V. I. Kolobov, Phys. Rev. Lett. **79**, 4589 (1997).
[15]P. M. Platzman and S. J. Buchsbaum, Phys. Rev. **128**, 1004 (1962).
[16]D. G. Swanson, *Plasma Waves* (Institute of Physics Publishing, London, United Kingdom, 2003).
[17]A. W. Degeling, C. O. Jung, R. W. Boswell, and A. R. Ellingboe, Phys. Plasmas **3**, 2788 (1996).
[18]A. W. Degeling, Ph. D. dissertation, Australian National University, 1999.
[19]F.F. Chen and R. W. Boswell, IEEE Trans. Plasma Sci. **25**, 1245 (1997).
[20]K. P. Shamrai and V. B. Taranov, Plasma Sources Sci. Technol. **5**, 474 (1996).
[21]C. L. Olson, Phys. Fluids **15**, 160 (1972).